

Lateral lattice coherence lengths in thin films of bismuth telluride topological insulators, with overview on polarization factors for X-ray dynamical diffraction in monochromator crystals

Sérgio L. Morelhão,^{*,†,‡} Stefan Kycia,^{*,†} Samuel Netzke,[†] Celso I. Fornari,[¶]
Paulo H. O. Rappl,[¶] and Eduardo Abramof[¶]

[†]*Department of Physics, University of Guelph, Guelph, Ontario N1G 1W2, Canada*

[‡]*Institute of Physics, University of São Paulo, São Paulo 05508-090, Brazil*

[¶]*National Institute for Space Research, São José dos Campos, São Paulo 12227-010, Brazil*

E-mail: morelhao@if.usp.br; skycia@uoguelph.ca

Abstract

In the supporting information file for article Dynamics of Defects in van der Waals Epitaxy of Bismuth Telluride Topological Insulators (J. Phys. Chem. C 2019, 123, 24818-24825, doi: 10.1021/acs.jpcc.9b05377), several topics on X-ray diffraction analysis of thin films were developed or revisited. A simple equation to determine lateral lattice coherence lengths in thin films stands as the main development (section S4 - Lateral lattice coherence length in thin films), while X-ray dynamical diffraction simulation in monochromator crystals stands as an interesting overview on how the ratio between π and σ polarization components is affected by whether diffraction takes place under kinematical or dynamical regime (section S3 - Polarization factor).

S1 - Choice of asymmetric reflections

All allowed hkl reflections measured in a recent work¹ are listed in Table S1. Forbidden reflections with khl indexes, $h\leftrightarrow k$ regarding those in the Table S1, have null structure factors. They were also measured due to twinned domains in the films that are 60° rotated in azimuth regarding the film main lattice.^{2,3}

Table S1: List of allowed reflections measured in a recent work.¹ Diffraction vector of modulus $Q = (4\pi/\lambda) \sin \theta$, instrumental angles θ (detector arm at 2θ), χ , and ϕ , incidence angle α_i , and polarization factor p from Eq. (S6). Structure factors F calculated for the Bi₂Te₃ crystal structure (lattice parameters $a = 4.382\text{\AA}$ and $c = 30.497\text{\AA}$)⁴ using resonant amplitudes^{5,6} and null Debye-Waller factors. $h_s k_s l_s$ stand for film reflection indexes regarding the substrate reciprocal lattice (only for the 1st reflections in column 1).

hkl	$Q (\text{\AA}^{-1})$	$\theta (^\circ)$	$\chi (^\circ)$	$\phi (^\circ)$	$\alpha_i (^\circ)$	p	$ F $	h_s	k_s	l_s
01 5/10 5/11 5	1.950	13.831	31.889	-60/60/180	7.26	0.679	815.0	1.25	-0.75	1.25
10 10/11 10/01 10	2.643	18.907	51.214	-120/0/120	14.63	0.642	725.5	0.51	0.51	2.51
20 5/22 5/02 5	3.468	25.160	17.280	-120/0/120	7.26	0.593	695.5	-0.75	-0.75	3.25
02 10/20 10/22 10	3.900	28.562	31.889	-60/60/180	14.63	0.567	637.6	2.51	-1.49	2.51
21 5/32 5/13 5	4.500	33.482	13.233	79/199/319	7.26	0.535	626.1	1.25	3.25	-2.75
21 10/32 10/13 10	4.841	36.403	25.189	-101/19/139	14.63	0.520	579.7	0.51	-1.49	4.51

For thin epitaxial films undergoing Kinematical diffraction, the integrated intensity of a Bragg reflection is proportional to the beam footprint on the film surface, Eq. (S2). Then, to improve accuracy in determining atomic displacement parameters from integrated intensity data, the preference is for sets of reflections that have a common incidence angle α_i . With the film surface normal direction $\hat{\mathbf{n}}$, set collinear to the ϕ rotation axis of the 4-circle goniometer (Fig. 2a in the main text), the incidence angle can be obtained from the goniometer angles as $\sin \alpha_i = \sin \theta \sin \chi$. When the diffraction vector \mathbf{Q} of an asymmetric reflection is placed in the incidence plane at the correct Bragg angle, $\sin \theta = (\lambda/4\pi)Q$ and $\sin \chi = \mathbf{Q} \cdot \hat{\mathbf{n}}/Q$, leading to

$$\sin \alpha_i = (\lambda/4\pi)\mathbf{Q} \cdot \hat{\mathbf{n}} = \lambda l/2c, \quad (\text{S1})$$

which is constant for all asymmetric reflections with the same l index in (001) films. Two sets of asymmetric reflections were chosen, hk5 and hk10 with incidence angles $\alpha_i = 7.26^\circ$ and 14.63° , respectively.

Besides reflections with a common angle of incidence, film reflections must be far away from the substrate reflections to avoid extra intensity contributions in the film rocking curves (θ -scans) for integrated intensity measurements. The relative orientation of film and substrate lattices, as depicted in Fig. S1, is such that all allowed hk5 and hk10 film reflections are aligned along the surface normal direction with substrate reflections. However, their reciprocal lattice points (RLPs) fall in between those from the substrate lattice at a minimum distance of $\Delta Q_z = 0.44 \text{ \AA}^{-1}$ in reciprocal space, Fig. S1(e). The closest substrate diffracted beam propagates at $\Delta\chi \approx 6^\circ$ from the incidence plane, as given by

$$\Delta\chi \simeq \mathbf{Q} \cdot \hat{\mathbf{n}}/Q - (\mathbf{Q} \cdot \hat{\mathbf{n}} - \Delta Q_z)/\sqrt{Q^2 + \Delta Q_z^2}$$

for $\mathbf{Q} = \bar{2}\mathbf{a}^* + \bar{1}\mathbf{b}^* + 5\mathbf{c}^*$ ($Q = 4.496 \text{ \AA}^{-1}$), which is easily cut off by the vertical acceptance of 0.6° of the detector system.

Choosing only reflections that have three-fold symmetry around the [001] direction is also important due to twinned domains often observed in the Bi_2Te_3 films. Since these domains are rotated by 60° in azimuth regarding the main lattice of the films, reflections with six-fold symmetry are inevitably mixing contributions from the main lattice and from twinned domains. On the other hand, allowed reflections such as 015, $\bar{1}05$, and $1\bar{1}5$ are set apart by 120° in azimuth, as given in Table S1, while reflections 105 , $0\bar{1}5$, and $\bar{1}\bar{1}5$ are forbidden, unless receiving intensity contributions from twinned domains.

S2 - Integrated intensity

In small single crystals and thin epitaxial films, atomic displacement values can be determined by measuring the diffraction power $P = \int I(\theta)d\theta = I_e|F|^2 N\lambda^3/\sin(2\theta) V_{\text{cel}}$ of different hkl reflections;⁵ it is also known as integrated intensity of the diffraction curve $I(\theta)$ as a function of the rocking curve angle θ . For thin films, this general expression can be written in terms of three parameters that are varying from one reflection to another: the scatter-

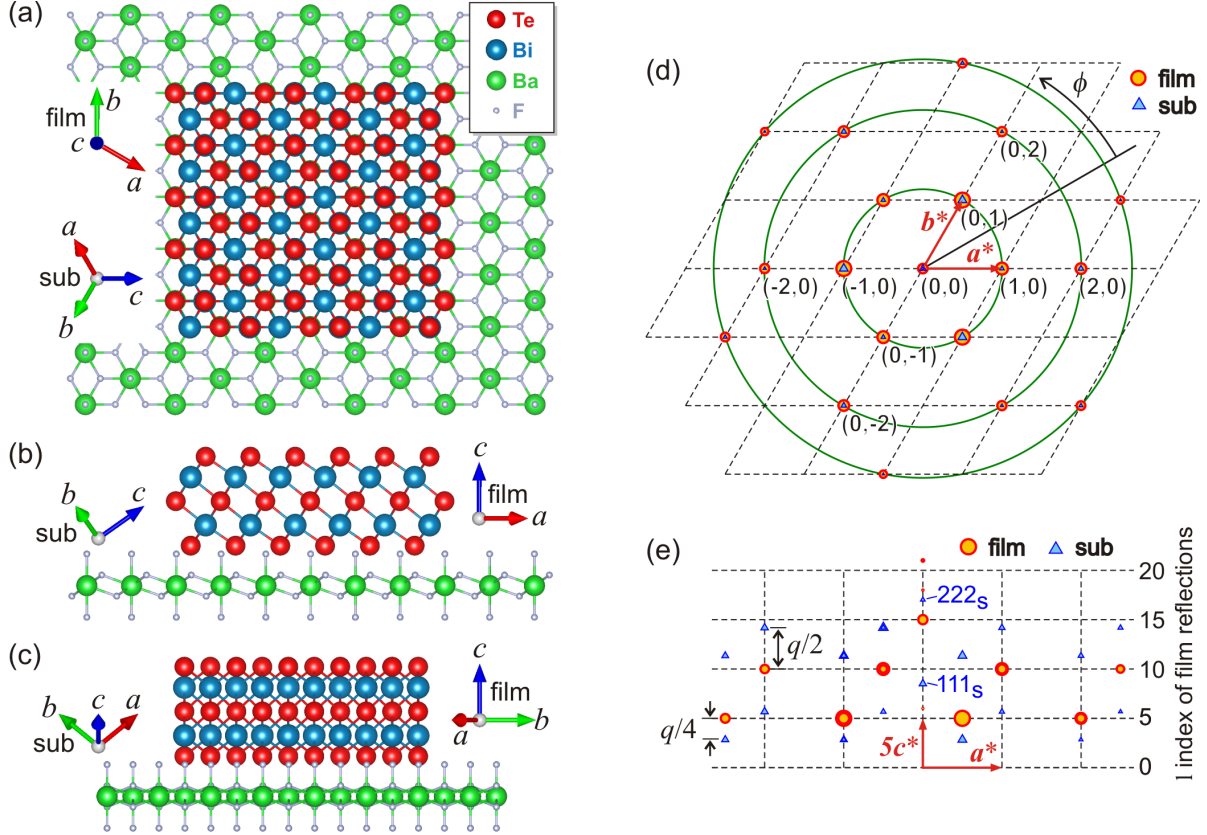


Figure S1: (a-c) Atomic arrangement of hexagonal Bi_2Te_3 film on cubic BaF_2 (111) substrate seen from different perspectives, as indicated by arrows along the basis vectors \mathbf{a} , \mathbf{b} , and \mathbf{c} of each lattice. (d,e) Film and substrate reciprocal lattice points (RLPs) according to the lattices relative orientation given in the left panels where $[110]\text{Bi}_2\text{Te}_3(001) \parallel [0\bar{1}1]\text{BaF}_2(111)$, azimuth $\phi = 0$. \mathbf{a}^* , \mathbf{b}^* , and \mathbf{c}^* stand for basis vectors of the film reciprocal lattice only. (d) In-plane viewing with RLPs connected by circles of radius $|\mathbf{h}\mathbf{a}^* + \mathbf{k}\mathbf{b}^*| = 1.654 \text{ \AA}^{-1}$, 3.308 \AA^{-1} , and 4.376 \AA^{-1} . (e) Film RLPs (orange circles) of the measured asymmetric reflections falling either at $1/4$ or $1/2$ of the distance $q = 2\pi/d_{111s} = 1.755 \text{ \AA}^{-1}$ between adjacent substrate RLPs (blue triangles) aligned along the surface normal direction.

ing angle 2θ , the structure factor F , and the number N of unit cells within the diffracting volume NV_{cell} for x-ray of wavelength λ . The scattering intensity by a single electron, I_e , also depends on 2θ through the polarization factor p since $I_e \propto p$. In thin films of uniform thickness and negligible absorption, N is proportional to the beam footprint $S_0/\sin\alpha_i$ for an incident x-ray beam of cross-section S_0 , leading to

$$P = C p |F|^2 / (\sin 2\theta \sin \alpha_i) \quad (\text{S2})$$

where C is a constant for each sample. Since the number of accessible reflections in thin films are limited, the atomic displacement parameters U_{ij} ,⁷ for all elements have been restricted to the diagonal terms only, $U_{11} = U_{22} = U_y$ and $U_{33} = U_z$ with respect to in-plane (or lateral) and longitudinal directions, respectively. With this restriction the structure factor expression simplifies to $F = \exp[-\frac{1}{2}(Q_y^2 U_y + Q_z^2 U_z)] \sum_a f_a \exp(i\mathbf{Q} \cdot \mathbf{r}_a)$ where the diffraction vector $\mathbf{Q} = h\mathbf{a}^* + k\mathbf{b}^* + l\mathbf{c}^*$ has been splitted into two components: $\mathbf{Q}_y = h\mathbf{a}^* + k\mathbf{b}^*$ in the plane of the film, Figure. S1(d), and $\mathbf{Q}_z = l\mathbf{c}^*$ along the growth direction. The corresponding root mean square (rms) atomic displacements are then $U_y^{1/2}$ (lateral) and $U_z^{1/2}$ (longitudinal). Data fitting of experimental integrated intensities (peak areas) were carried out by using a simulated annealing (SA) algorithm^{8,9} to adjust C , U_y , and U_z in the above equation, Eq. (S2). These fitting parameters were adjusted by minimizing the mean squared logarithmic error (MSLE) $E = \frac{1}{N_j} \sum_j \ln^2 [P_j/P_s(\mathbf{Q}_j, C, U_y, U_z)]$ where P_j and $P_s(\mathbf{Q}_j, C, U_y, U_z)$ are experimental and simulated data points for each j -th reflection of diffraction vector \mathbf{Q}_j in the set of N_j reflections. After minimizing the MSLE function, relative variation of the experimental data due to atomic displacements have been displayed in the main text as

$$\Delta P/P = \frac{P_j - P_s(\mathbf{Q}_j, C, 0, 0)}{P_s(\mathbf{Q}_j, C, 0, 0)}. \quad (\text{S3})$$

S3 - Polarization factor

Unpolarized x-rays of wavevector $\mathbf{K} = (2\pi/\lambda)\hat{\mathbf{s}}$, after scattering by electrons into wavevector $\mathbf{K}' = (2\pi/\lambda)\hat{\mathbf{s}}'$ have polarization factor $p(2\theta) = \langle |\mathcal{P}|^2 \rangle$ where

$$\mathcal{P} = \hat{\mathbf{s}}' \times (\hat{\boldsymbol{\varepsilon}} \times \hat{\mathbf{s}}') \quad (\text{S4})$$

stands for each linearly polarized component of the incident wavefield vibrating along direction $\hat{\boldsymbol{\varepsilon}} = \cos(\varepsilon)\hat{\boldsymbol{\pi}} + \sin(\varepsilon)\hat{\boldsymbol{\sigma}}$.^{5,10-12} The two orthogonal components have been defined as $\hat{\boldsymbol{\pi}} = \hat{\boldsymbol{\sigma}} \times \hat{\mathbf{s}}$ and $\hat{\boldsymbol{\sigma}} = \hat{\mathbf{s}} \times \hat{\mathbf{s}}' / \sin(2\theta)$. By using $\hat{\mathbf{s}} = \hat{\mathbf{z}}$ and $\hat{\mathbf{s}}' = \sin(2\theta)\hat{\mathbf{x}} + \cos(2\theta)\hat{\mathbf{z}}$, we have that $\mathcal{P} = \cos(\varepsilon)\cos^2(2\theta)\hat{\mathbf{x}} + \sin(\varepsilon)\hat{\mathbf{y}} - \cos(\varepsilon)\cos(2\theta)\sin(2\theta)\hat{\mathbf{z}}$. Since $\langle \cos^2(\varepsilon) \rangle = \langle \sin^2(\varepsilon) \rangle = 1/2$ for ε varying from 0 to 2π in the unpolarized beam, $p(2\theta) = [1 + \cos^2(2\theta)]/2$ is the well known polarization factor for scattering of unpolarized x-rays. It is also the polarization factor in the case of x-ray diffraction in small crystals such as thin epitaxial films diffracting according to the Kinematical theory. In large crystals such as the monochromator crystals undergoing a single Bragg reflection in reflection geometry, the intensity ratio $R_{\pi\sigma}$ between the π and σ components in the diffracted beam is affected by crystalline perfection and x-ray absorption that can be different for each of these components.¹³ The exact polarization factor for a perfect Ge 220 monochromator and $\text{CuK}_{\alpha 1}$ radiation, $\theta_{220}^{\text{Ge}} = 22.6484^\circ$, can be obtained by dynamical diffraction simulation,¹⁴ as shown in Fig. S2. For very thin crystals ($< 0.1 \mu\text{m}$) or crystals with damaged surface diffracting kinematically, $R_{\pi\sigma} \simeq \cos^2(2\theta_{220}^{\text{Ge}}) = 0.495$, while for perfect thick crystals ($> 5 \mu\text{m}$), $R_{\pi\sigma} = 0.675 < \cos(2\theta_{220}^{\text{Ge}})$.

After the double collimating multilayer optic of the used diffractometer, the x-ray beam is still unpolarized before hitting the monochromator. In total, the detected x-rays undergo three Bragg reflections, two inside the monochromator and one in the sample, as depicted in Fig. S3. Then, the above equation, Eq. (S4), has to be applied recursively to each reflection, resulting in

$$\mathcal{P}_n = \hat{\mathbf{s}}'_n \times (\mathcal{P}_{n-1} \times \hat{\mathbf{s}}'_n) \quad (\text{S5})$$

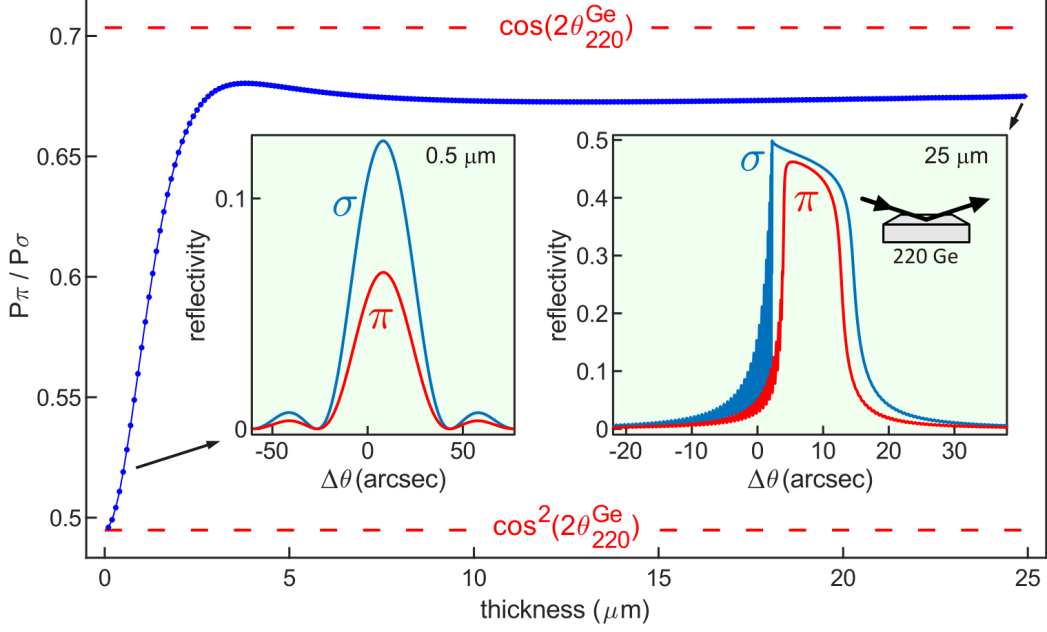


Figure S2: For a single 220 Ge Bragg reflection, ratio $R_{\pi\sigma}$ between integrated reflectivities P_π and P_σ of each polarization component in the diffracted beam as a function of crystal thickness. $\text{CuK}_{\alpha 1}$ radiation ($\theta_{220}^{\text{Ge}} = 22.6484^\circ$) with 45° linearly polarized incident beam, i.e. $\hat{\epsilon} = \cos(45^\circ)\hat{\pi} + \sin(45^\circ)\hat{\sigma}$ in Eq. (S4). Examples of reflectivity curves from dynamic diffraction simulation¹⁴ are given in the insets. For crystals undergoing kinematic diffraction $R_{\pi\sigma} = \cos^2(2\theta_{220}^{\text{Ge}})$, while under dynamical regime of diffraction $R_{\pi\sigma} \lesssim \cos(2\theta_{220}^{\text{Ge}})$.

where $\mathcal{P}_0 = \hat{\epsilon}$ and $n = 1, 2, 3$. By taking $R_{\pi\sigma}$ as the reduction ratio in the π component after each 220 Ge reflection inside the monochromator, and θ_{hkl} as the Bragg angle of reflection hkl in the film,

$$p(2\theta_{\text{hkl}}) = [1 + R_{\pi\sigma}^2 \cos^2(2\theta_{\text{hkl}})] / 2 \quad (\text{S6})$$

is the final polarization factor to be used when calculating the integrated intensities of the film's hkl reflections. It implies that, the monochromator delivers x-rays with a relative amount $R_{\pi\sigma}^2$ of polarization in the incidence plane of the diffractometer. This component of π -polarization is the fraction of incident x-rays in the sample that are in fact susceptible to the diffraction angle $2\theta_{\text{hkl}}$ of the film reflections. Without accounting for polarization in the monochromator ($R_{\pi\sigma}^2 = 1$), there would be a much more drastic reduction in the relative values of integrated intensities as the diffraction angle increases, as shown in Fig. S4. With the two-reflection monochromator, the relative amount of π -polarization is in the range

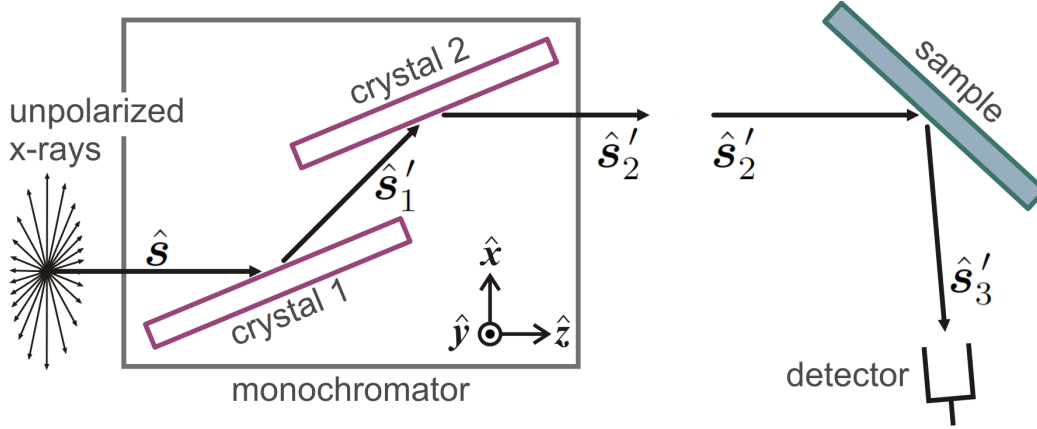


Figure S3: Bragg reflections along the beam path from unpolarized x-rays before the monochromator until detection after the sample. Each reflection changes the beam direction to \hat{s}'_n and polarization according to Eq. (S5), leading to the polarization factor $p(2\theta_{hkl})$ in Eq. (S6).

$0.25 \leq R_{\pi\sigma}^2 \lesssim 0.46$ depending on the diffraction regime (kinematical or dynamical) of the monochromator crystals. The in-plane rms atomic displacement values reported in a recent work¹ were determined for $R_{\pi\sigma}^2 = 0.46$ and the polarization factors listed in Table S1. By using $R_{\pi\sigma}^2 = 0.25$ instead (kinematical approach), all values are evenly increased by about 2 pm within the same error bars, i.e. $U_y^{1/2} = 14.8$ pm, 14.1 pm, 13.9 pm, and 14.1 pm would be 16.6 pm, 16.0 pm, 15.8 pm, and 15.9 pm, respectively.

S4 - Lateral lattice coherence length in thin films

Intensity distribution around reciprocal lattice points (RLPs) are related by Fourier transform to lattice coherence lengths inside the diffracting volume. In a perfect crystal domain, the coherence lengths are the sizes of the domain itself. But in epitaxial films, elastic strain and defects due to accommodation of lattice misfit at the film-substrate interface can lead to coherence lengths smaller than the sizes of the crystallographic domains. In other words, lattice coherence lengths can be smaller than domain sizes seen by morphological probes such as atomic force microscopy.

For diffraction vectors \mathbf{Q} of asymmetric reflections, the film coherence lengths L_x , L_y ,

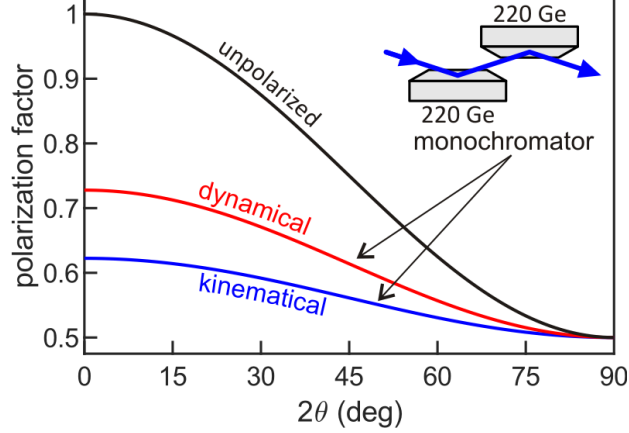


Figure S4: Polarization factor as a function of the diffracted beam angle 2θ in the film reflections. Calculation for a two-reflection monochromator (inset) when using $R_{\pi\sigma}^2 = 0.46$ (dynamical) or 0.25 (kinematical) in Eq. (S6). For sake of comparison, the polarization factor for unpolarized radiation, i.e. without the monochromator ($R_{\pi\sigma}^2 = 1$), is also shown.

and L_z are related to RLP broadening along in-plane directions

$$\hat{\mathbf{x}} = \hat{\mathbf{z}} \times \mathbf{Q} / |\hat{\mathbf{z}} \times \mathbf{Q}| \quad \text{and} \quad \hat{\mathbf{y}} = \hat{\mathbf{z}} \times \hat{\mathbf{x}}, \quad (\text{S7})$$

as well as along the growth direction $\hat{\mathbf{z}}$, respectively. In diffraction geometry for very asymmetric reflections, as in Fig. S5(a) where $\chi \ll 90^\circ$, peak widths in rocking curve measurements (θ -scans) are most susceptible to the RLP broadening along in-plane directions, Eq. (S7), since along the crystal truncation rod, *i.e.* along $\hat{\mathbf{z}}$, it is nearly perpendicular to the incidence plane.

Lattice imperfections with Burgers vectors parallel to the Bragg plane are invisible to the corresponding Bragg reflection,¹⁵ producing no reduction of coherence lengths perpendicular to the diffraction vector, as in the case of L_x for which $\mathbf{Q} \cdot \hat{\mathbf{x}} = 0$. On the other hand, misfit of film/substrate parameters reduces the coherence length L_y according to the average lattice imperfection separation distance^{16,17}

$$\bar{s} = \frac{a_s}{\varepsilon_0 + |\Delta a/a|} \quad (\text{S8})$$

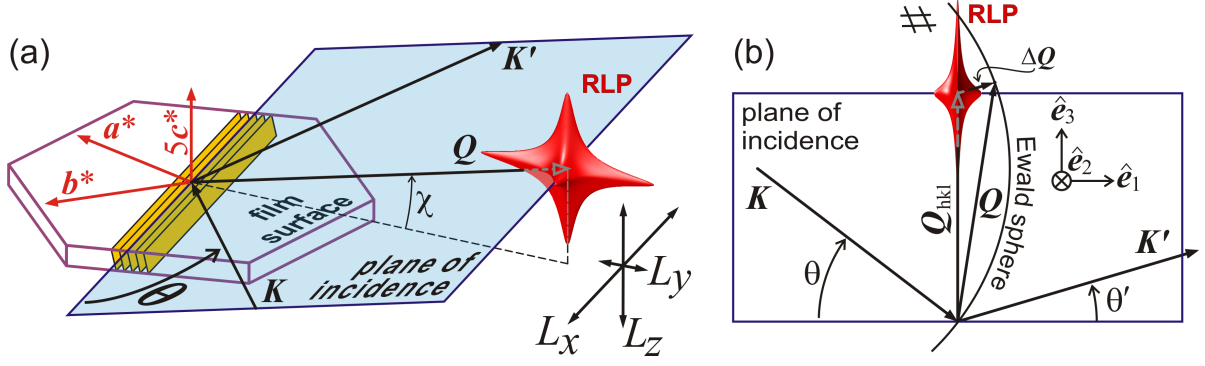


Figure S5: (a) Diffraction geometry of asymmetric reflection with diffraction vector $\mathbf{Q} = \mathbf{K}' - \mathbf{K}$ at an angle χ from the film surface. Broadening of reciprocal lattice point (RLP) due to finite lattice coherence lengths L_x and L_y (along film in-plane directions), and L_z (along the film growth direction). Hexagonal film with basis vectors \mathbf{a}^* , \mathbf{b}^* , and \mathbf{c}^* of the reciprocal lattice. (b) Vectors, angles, and frame definitions used for calculating peak widths in rocking curve measurements (θ -scans) around the reciprocal lattice vector $\mathbf{Q}_{hkl} = h\mathbf{a}^* + k\mathbf{b}^* + l\mathbf{c}^*$ of reflection hkl.

where ε_0 is the amount of misfit strain elastically accommodated in the absence of lattice mismatch $\Delta a/a = (a_f - a_s)/a_s$, regarding the actual film and substrate lateral lattice parameters present in the sample, a_f and a_s respectively.

In rocking curve measurements, diffraction peak widths are determined by the convolution between Ewald sphere and RLP as a function of the rocking angle θ . If function $|W(\Delta\mathbf{Q})|^2$ describes the RLP broadening in reciprocal space, line profile of diffraction peaks can be calculated as⁵

$$I(\theta) = \iint |W(\Delta\mathbf{Q})|^2 \sin \theta' d\theta' d\varphi' \quad (\text{S9})$$

where $\Delta\mathbf{Q} = \mathbf{Q} - \mathbf{Q}_{hkl} = [\mathbf{K}'(\theta', \varphi') - \mathbf{K}(\theta)] - \mathbf{Q}_{hkl}$ is the distance from the centre of the RLP given by the reciprocal lattice vector \mathbf{Q}_{hkl} of reflection hkl. For an incident wavevector written as

$$\mathbf{K} = (2\pi/\lambda)[\cos \theta \hat{\mathbf{e}}_1 - \sin \theta \hat{\mathbf{e}}_3]$$

in the reference frame $[\hat{\mathbf{e}}_1, \hat{\mathbf{e}}_2, \hat{\mathbf{e}}_3]$ of the incidence plane, as defined in Fig. S5(b) where $\mathbf{Q}_{hkl} = Q_{hkl}\hat{\mathbf{e}}_3$, all physically possible wavevectors of diffracted x-rays (elastic scattering

process) are accounted for as

$$\mathbf{K}' = (2\pi/\lambda)[\cos \theta' \hat{\mathbf{e}}_1 + \sin \theta' \sin \varphi' \hat{\mathbf{e}}_2 + \sin \theta' \cos \varphi' \hat{\mathbf{e}}_3],$$

even those rays going out of the incidence plane for which angle $\varphi' \neq 0$. Projection of $\Delta\mathbf{Q}$ in the xyz frame earlier defined in Eq. (S7) is provided by

$$\hat{\mathbf{e}}_1 = \hat{\mathbf{x}}, \quad \hat{\mathbf{e}}_2 = \sin \chi \hat{\mathbf{y}} + \cos \chi \hat{\mathbf{z}}, \quad \text{and} \quad \hat{\mathbf{e}}_3 = -\cos \chi \hat{\mathbf{y}} + \sin \chi \hat{\mathbf{z}}, \quad (\text{S10})$$

allowing the RLP broadening due to finite lattice coherence lengths along $\Delta Q_x = \Delta\mathbf{Q} \cdot \hat{\mathbf{x}}$, $\Delta Q_y = \Delta\mathbf{Q} \cdot \hat{\mathbf{y}}$, and $\Delta Q_z = \Delta\mathbf{Q} \cdot \hat{\mathbf{z}}$ to be taken into account for asymmetric reflections with diffraction vector at an angle χ from the film surface, Fig. S5(a).

In one dimension, the Fourier transform of a finite lattice of length L is the sinc function $\sin(\Delta Q L/2)/(\Delta Q/2)$.⁵ Then, the modulus square of the normalized function

$$W(\Delta\mathbf{Q}) = \frac{\sin(\Delta Q_x L_x/2)}{\Delta Q_x L_x/2} \frac{\sin(\Delta Q_y L_y/2)}{\Delta Q_y L_y/2} \frac{\sin(\Delta Q_z L_z/2)}{\Delta Q_z L_z/2}. \quad (\text{S11})$$

has been chosen to describe the intensity distribution around the RLPs in Eq. (S9). Although it is possible to fit experimental peak widths by handling numerically the double integral in Eq. (S9), determination of the coherence lengths $L_{x,y,z}$ with this procedure can be very time consuming. Here, a different approach has been developed. Squared sinc functions have full width at half maximum (fwhm) given by $\beta_{x,y,z} = 5.566/L_{x,y,z}$ (numerator comes from $\sin^2(x)/x^2 = 1/2$ when $4x = 5.566$), which were projected in the incidence plane, and the corresponding peak widths $\Delta\theta_{x,y,z}$ in θ -scans obtained by using standard 2D Ewald construction in reciprocal space, *e.g.* Fig. S5(b). The resulting peak width is then calculated as

$$w_S = \sqrt{\Delta\theta_x^2 + \Delta\theta_y^2 + \Delta\theta_z^2} \quad (\text{S12})$$

where $\Delta\theta_x = \beta_x/Q_{\text{hkl}}$, $\Delta\theta_y = \beta_y \tan \theta \cos \chi/Q_{\text{hkl}}$, and $\Delta\theta_z = \beta_z \tan \theta \sin \chi/Q_{\text{hkl}}$. In Fig. S6

there is a comparison of peak widths calculated by the exact solution in Eq. (S9) and by the approach in Eq. (S12). Since the latter approach shows very good agreement with the exact solution and is much faster in terms of CPU time, it has been used to determine the coherence lengths from the experimental peak widths.

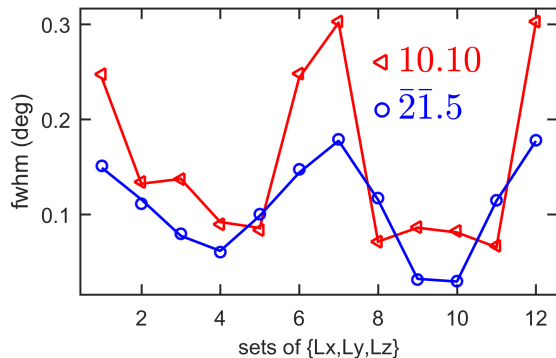


Figure S6: Comparison of peak widths (fwhm) from exact solution (symbols) in Eq. (S9) and the proposed approach (solid lines) in Eq. (S12). The 10 10 and $\bar{2}1\bar{5}$ reflections stand for the least and the most asymmetric ones listed in Table S1. $\{L_x, L_y, L_z\}$ (nm) = $\{50, 100, 200\}$, $\{100, 50, 200\}$, $\{100, 200, 50\}$, $\{200, 100, 50\}$, $\{200, 50, 100\}$, $\{50, 200, 100\}$, $\{40, 400, 2000\}$, $\{400, 40, 2000\}$, $\{400, 2000, 40\}$, $\{2000, 400, 40\}$, $\{2000, 40, 400\}$, and $\{40, 2000, 400\}$ were the sets of coherence lengths used for this test, 1, 2, . . . , 12, respectively.

Coherence length values were adjusted by SA algorithm to minimize the mean square deviation function $\sigma^2 = \sum_j (w_E - w_S)_j^2 / N_j$ where w_E and w_S stand for experimental and calculated peak widths, respectively. w_S is obtained from Eq. (S12). Subscript j runs over the $N_j = 3$ reflections in either hk5 and hk10 subsets of reflections. Uncertainties $\pm\sigma_L$ were estimated from the error bars σ_w in w_E values as $(\sigma_L/L)^2 = \sum_j (\sigma_w/w_E)_j^2$. The standard errors σ_w were obtained by measuring a few times equivalent reflections set apart by 120° in azimuth (Table S1).

S5 - Hybrid reflections

Hybrid reflections have been studied and applied to investigate heteroepitaxial systems since 1981.^{18–29} However, only recently their occurrence in epitaxial systems of hexagonal (001) films on cubic (111) substrates, such as $\text{Bi}_2\text{Te}_3/\text{BaF}_2$, have been predicted and observed at

scattering angles³⁰

$$2\theta_{n,m} = 2 \arcsin \left[\frac{\lambda}{2} \left(\frac{n}{a\sqrt{3}} + \frac{m}{c} \right) \right] \quad (\text{S13})$$

where $n = \sum_s (h_s + k_s + l_s) > 0$ and $m = \sum_f l_f$. For the pair of hybrid reflections recently measured,¹ hybrids $\bar{2}2.\bar{1}0_f + 044_s$ (peak f/s) and $404_s + 0\bar{2}.\bar{1}0_f$ (peak s/f), both have $n = 8$ and $m = -10$. By using $a = 6.2001 \text{ \AA}$ as the cubic lattice parameter of BaF_2 and $c = 30.497 \text{ \AA}$ as the hexagonal lattice parameter of the film, $\theta_{8,-10} = 18.74^\circ$ is close to the incidence angle used to excite these hybrids in symmetric diffraction geometry. However, each hybrid occurs at different azimuth. For the reference of azimuth defined in Fig. S1, peak f/s is centred at about $\varphi = 53.6^\circ$ and peak s/f at $\varphi = 66.4^\circ$. Meshscans in θ and φ were carried out around these azimuths to properly determine the hybrid peak position in θ ; a detailed description on how to measure such hybrids can be found elsewhere.³⁰ The split of a hybrid pair as function of the rocking curve angle θ is proportional to $\Delta a/a$ as given by

$$\Delta\theta \simeq -2 \frac{\mathbf{Q}_{f,\parallel} \cdot \hat{\mathbf{k}}_{\parallel}}{Q^*} \frac{\Delta a}{a}. \quad (\text{S14})$$

$\mathbf{Q}_{f,\parallel}$ is the in-plane component of the film diffraction vector and $\hat{\mathbf{k}}_{\parallel}$ is the in-plane direction of the incident wavevector. For the case of hybrids $\bar{2}2.\bar{1}0_f + 044_s$ (peak f/s) and $404_s + 0\bar{2}.\bar{1}0_f$ (peak s/f), $\mathbf{Q}_{f,\parallel} \cdot \hat{\mathbf{k}}_{\parallel}/Q^* = 1.0176$, which leads to the values of $\Delta a/a$ reported here.

S6 - Film composition

Films with composition $(\text{Bi}_2)_M(\text{Bi}_2\text{Te}_3)_N$ have deficit $\delta = 3M/(N + M)$ of tellurium due to formation of bismuth bilayers (BLs) in the vdW gap between adjacent quintuple layers (QLs). X-ray diffraction simulation in model structures containing a number M of BLs randomly distributed along the film thickness have been used to determine the actual composition of the films.^{4,31,32} In first order approximation, variation of interlayer spacing in the model structures as a function of δ were accounted for as shown in Fig. S7. By comparing

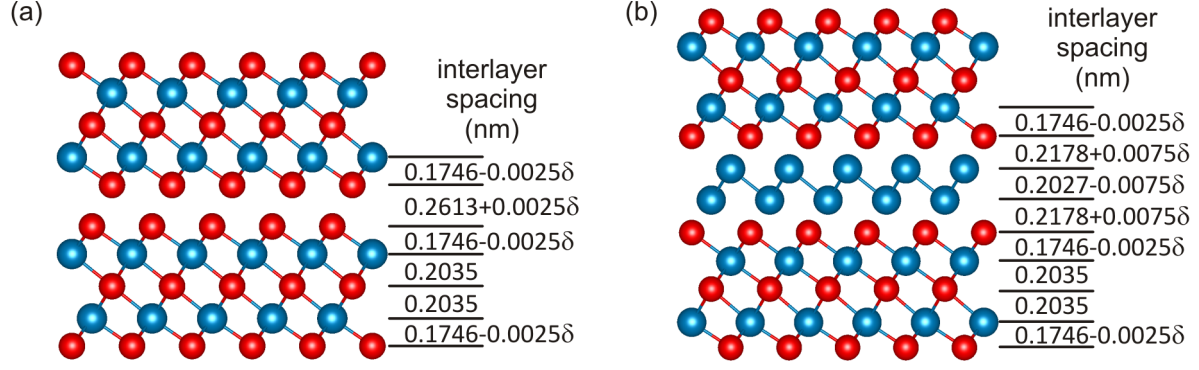


Figure S7: Interlayer spacing for model structures as a function of Te deficit δ in films with composition $\text{Bi}_2\text{Te}_{3-\delta}$. (a) Around the vdW gap between adjacent QLs, and (b) when a bismuth bilayer (BL) is formed in the vdW gap. First order approximation of structural strain caused by the presence of BLs (see Appendix of Ref. 29 for more details).

experimental and simulated x-ray diffraction curves in Fig. S8, only two samples present features owing to the presence of BLs: shifting of peak 00 15 whose position is determined by the mean interlayer spacing $\langle d \rangle \simeq 0.2035 - 0.0025\delta$;^{2,4} and splitting of peak 00 18 (shaded area in Fig. S8(b)) that is also proportional to δ according to $(2\pi/\lambda) \cos \theta \Delta 2\theta = 0.23 \delta$ (for $\Delta 2\theta$ in radians).^{2,31} By using this later formula with the values indicated in Fig. S8(a), samples S17n and S19n have films of compositions $\text{Bi}_2\text{Te}_{2.74}$ and $\text{Bi}_2\text{Te}_{2.58}$, respectively.

References

1. Morelhão, S. L.; Kycia, S. W.; Netzke, S.; Fornari, C. I.; Rappl, P. H. O.; Abramof, E. Dynamics of Defects in van der Waals Epitaxy of Bismuth Telluride Topological Insulators. *J. Phys. Chem. C* **2019**, *123*, 24818–24825.
2. Fornari, C. I.; Rappl, P. H. O.; Morelhão, S. L.; Abramof, E. Structural Properties of Bi_2Te_3 Topological Insulator Thin Films Grown by Molecular Beam Epitaxy on (111) BaF_2 Substrates. *J. Appl. Phys.* **2016**, *119*, 165303.
3. Fornari, C. I.; Rappl, P. H. O.; Morelhão, S. L.; Peixoto, T. R. F.; Bentmann, H.; Reinert, F.; Abramof, E. Preservation of Pristine Bi_2Te_3 Thin Film Topological Insulator

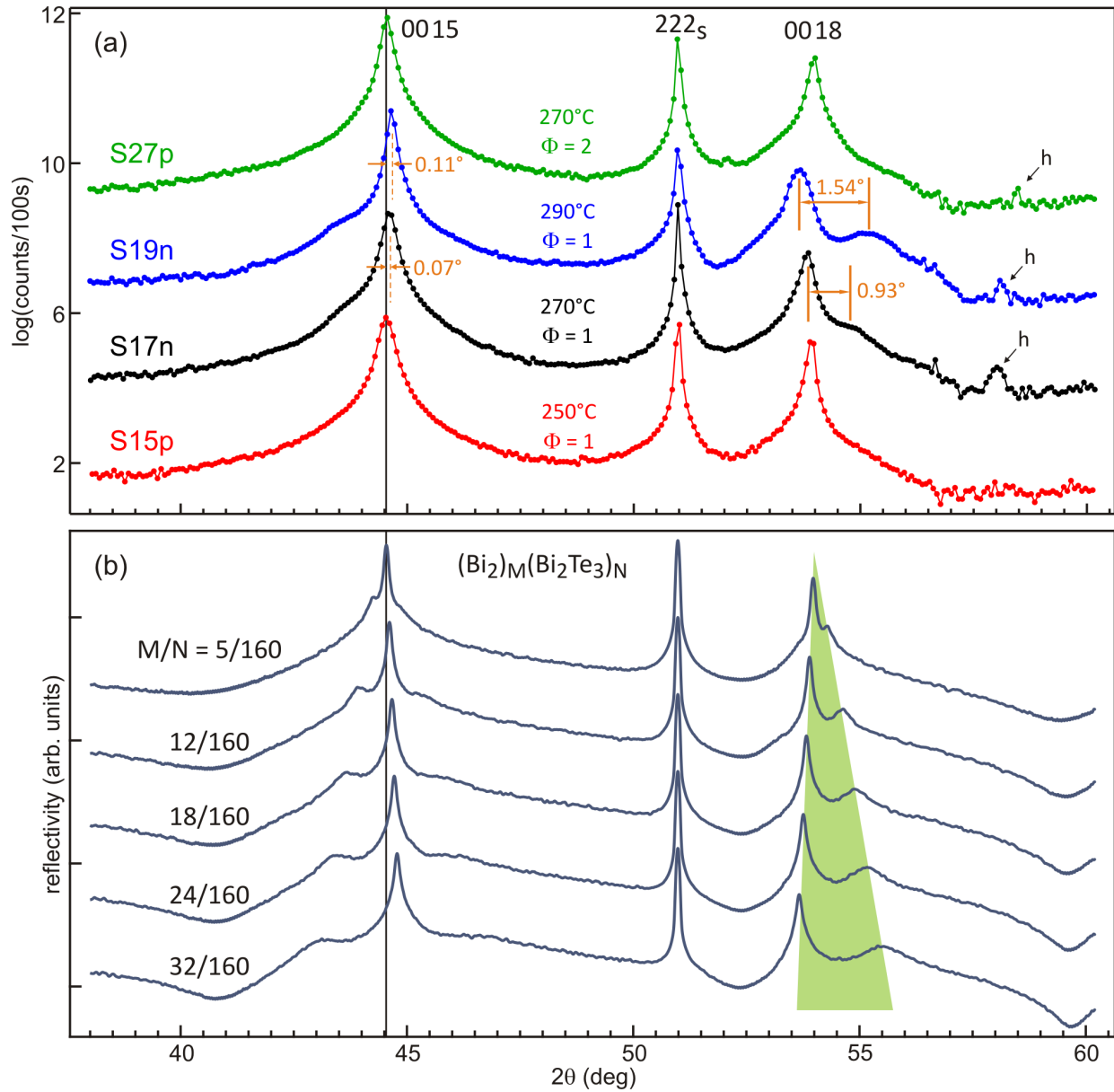


Figure S8: (a) $\theta/2\theta$ -scans along the c -axis of Bi_2Te_3 films on BaF_2 (111) substrates. X-rays of $\lambda = 1.540562 \text{ \AA}$ ($\text{CuK}\alpha_1$). Sample labels, substrate temperature during film growth, and ratio Φ between beam equivalent pressures of Te and Bi_2Te_3 sources are indicated at each curve. Small peaks of hybrid reflections are seen (arrows h).³⁰ Shifting of 00 15 film reflection towards the 222_s substrate reflection, as well as splitting of 00 18 reflection peak, are due to the presence of BLs in the film structure. (b) Simulation of $\theta/2\theta$ -scans for $(\text{Bi}_2)_M(\text{Bi}_2\text{Te}_3)_N$ films with number M of BLs per number N of QLs by using a recursive series for x-ray dynamical diffraction calculation, as introduced elsewhere.³¹ The splitting of peak 00 18 (shaded area) is proportional to the content of BLs or, equivalently, to the Te deficit δ in $\text{Bi}_2\text{Te}_{3-\delta}$. It leads to 15/160 ($\delta \simeq 0.26$) and 26/160 ($\delta \simeq 0.42$) as the relative number M/N of BLs in the samples S17n and S19n, respectively.

- Surface After ex Situ Mechanical Removal of Te Capping Layer. *APL Mater.* **2016**, *4*, 106107.
4. Steiner, H.; Volobuev, V.; Caha, O.; Bauer, G.; Springholz, G.; Holý, V. Structure and Composition of Bismuth Telluride Topological Insulators Grown by Molecular Beam Epitaxy. *J. Appl. Cryst.* **2014**, *47*, 1889–1900.
 5. Morelhão, S. L. *Computer Simulation Tools for X-ray Analysis*; Graduate Texts in Physics; Springer, Cham, 2016.
 6. University of São Paulo, Department of Applied of Physics. <http://xraybook.if.usp.br/>, routine `fpfpp.m` (accessed March 10, 2018).
 7. Kuhs, W. F. In *International Tables for Crystallography Volume D: Physical properties of crystals*; Authier, A., Ed.; Springer: Netherlands, Dordrecht, 2003; pp 228–242.
 8. Kirkpatrick, S.; Gelatt, C. D.; Vecchi, M. P. Optimization by Simulated Annealing. *Science* **1983**, *220*, 671–680.
 9. Kabova, E. A.; Cole, J. C.; Korb, O.; López-Ibáñez, M.; Williams, A. C.; Shankland, K. Improved Performance of Crystal Structure Solution from Powder Diffraction Data Through Parameter Tuning of a Simulated Annealing Algorithm. *J. Appl. Cryst.* **2017**, *50*, 1411–1420.
 10. Morelhão, S. L.; Avanci, L. H. Strength Tuning of Multiple Waves in Crystals. *Acta Cryst. A* **2001**, *57*, 192–196.
 11. Morelhão, S. L.; Kycia, S. Enhanced X-ray Phase Determination by Three-Beam Diffraction. *Phys. Rev. Lett.* **2002**, *89*, 015501.
 12. Morelhão, S. L.; Remédios, C. M. R.; Freitas, R. O.; dos Santos, A. O. X-ray Phase Measurements as a Probe of Small Structural Changes in Doped Nonlinear Optical Crystals. *J. Appl. Cryst.* **2011**, *44*, 93–101.

13. Authier, A. *Dynamical Theory of X-Ray Diffraction*; Oxford University Press, Oxford, 2003.
14. Weckert, E.; Hümmer, K. Multiple-Beam X-ray Diffraction for Physical Determination of Reflection Phases and its Applications. *Acta Cryst. A* **1997**, *53*, 108–143.
15. Morelhão, S. L.; Härtwig, J.; Meier, D. L. Dislocations in Dendritic Web Silicon. *J. Cryst. Growth* **2000**, *213*, 288–298.
16. Merwe, J. H. V. D. The Role of Lattice Misfit in Epitaxy. *Crit. Rev. Solid State* **1978**, *7*, 209–231.
17. Herman, M. A.; Richter, W.; Sitter, H. *Epitaxy: Physical Principles and Technical Implementation*; Springer: Berlin, Heidelberg, 2004; pp 389–421.
18. Isherwood, B. J.; Brown, B. R.; Halliwell, M. A. G. X-ray Multiple Diffraction as a Tool for Studying Heteroepitaxial Layers. *J. Cryst. Growth* **1981**, *54*, 449–460.
19. Morelhão, S. L.; Cardoso, L. P. Simulation of Hybrid Reflections in X-ray Multiple Diffraction Experiments. *J. Cryst. Growth* **1991**, *110*, 543–552.
20. Morelhão, S. L.; Cardoso, L. P. Analysis of Interfacial Misfit Dislocation by X-ray Multiple Diffraction. *Solid State Commun.* **1993**, *88*, 465–469.
21. Morelhão, S. L.; Cardoso, L. P. Structural Properties of Heteroepitaxial Systems Using Hybrid Multiple Diffraction in Renninger Scans. *J. Appl. Phys.* **1993**, *73*, 4218–4226.
22. Morelhão, S. L.; Avanci, L. H.; Hayashi, M. A.; Cardoso, L. P.; Collins, S. P. Observation of Coherent Hybrid Reflection with Synchrotron Radiation. *Appl. Phys. Lett.* **1998**, *73*, 2194–2196.
23. Morelhão, S. L.; Quivy, A. A.; Härtwig, J. Hybrid and Effective Satellites for Studying Superlattices. *Microelectron. J.* **2003**, *34*, 695–699.

24. Morelhão, S. L.; Domagała, J. Z. Hybrid Reciprocal Space for X-ray Diffraction in Epitaxial Layers. *J. Appl. Cryst.* **2007**, *40*, 546–551.
25. Menezes, A. S.; dos Santos, A. O.; Almeida, J. M. A.; Bortoleto, J. R. R.; Cotta, M. A.; Morelhão, S. L.; Cardoso, L. P. Hybrid Reflections in InGaP/GaAs(001) by Synchrotron Radiation Multiple Diffraction. *Phys. Status Solidi B* **2009**, *246*, 544–547.
26. Menezes, A. S.; dos Santos, A. O.; Almeida, J. M. A.; Bortoleto, J. R. R.; Cotta, M. A.; Morelhão, S. L.; Cardoso, L. P. Direct Observation of Tetragonal Distortion in Epitaxial Structures Through Secondary Peak Split in a Synchrotron Radiation Renninger Scan. *Cryst. Growth Des.* **2010**, *10*, 3436–3441.
27. Domagała, J. Z.; Morelhão, S. L.; Sarzyński, M.; Maździarz, M.; Dłużewski, P.; Leszczyński, M. Hybrid Reciprocal Lattice: Application to Layer Stress Determination in GaAlN/GaN(0001) Systems with Patterned Substrates. *J. Appl. Cryst.* **2016**, *49*, 798–805.
28. Smith, E. H.; King, P. D. C.; Soukiassian, A.; Ast, D. G.; Schlom, D. G. Hybrid Reflections from Multiple X-ray Scattering in Epitaxial Oxide. *Appl. Phys. Lett.* **2017**, *111*, 131903.
29. de Prado, E.; Martínez-Tomás, M. C.; Deparis, C.; Muñoz-Sanjosé, V.; Zúñiga-Pérez, J. Hybrid Multiple Diffraction in Semipolar Wurtzite Materials. *J. Appl. Cryst.* **2017**, *50*, 1165–1173.
30. Morelhão, S. L.; Kycia, S.; Netzke, S.; Fornari, C. I.; Rappl, P. H. O.; Abramof, E. Hybrid Reflections from Multiple X-ray Scattering in Epitaxial Bismuth Telluride Topological Insulator Films. *Appl. Phys. Lett.* **2018**, *112*, 101903.
31. Morelhão, S. L.; Fornari, C. I.; Rappl, P. H. O.; Abramof, E. Nanoscale Characterization of Bismuth Telluride Epitaxial Layers by Advanced X-ray Analysis. *J. Appl. Cryst.* **2017**, *50*, 399–410.

32. Springholz, G.; Wimmer, S.; Groiss, H.; Albu, M.; Hofer, F.; Caha, O.; Kriegner, D.; Stangl, J.; Bauer, G.; Holý, V. Structural Disorder of Natural Bi_mSe_n Superlattices Grown by Molecular Beam Epitaxy. *Phys. Rev. Materials* **2018**, *2*, 054202.